Nanopurification of silicon from 84% to 99.999% purity with a simple and scalable process

Linqi Zong[a], Bin Zhu[a], Zhenda Lu[b], Yingling Tan[a], Yan Jin[a], Nian Liu[b], Yue Hu[a], Shuai Gu[a], Jia Zhu[a,1], and Yi Cui[b,c,1]

[a]National Laboratory of Solid State Microstructures, College of Engineering and Applied Sciences and Collaborative Innovation Center of Advanced Microstructures, Nanjing University, Nanjing 210093, China; [b]Department of Materials Science and Engineering, Stanford University, Stanford, CA 94305; and [c]Stanford Institute for Materials and Energy Sciences, Stanford Linear Accelerator Center National Accelerator Laboratory, Menlo Park, CA 94025

Edited by Charles M. Lieber, Harvard University, Cambridge, MA, and approved September 18, 2015 (received for review July 2, 2015)

Silicon, with its great abundance and mature infrastructure, is a foundational material for a range of applications, such as electronics, sensors, solar cells, batteries, and thermoelectrics. These applications rely on the purification of Si to different levels. Recently, it has been shown that nanosized silicon can offer additional advantages, such as enhanced mechanical properties, significant absorption enhancement, and reduced thermal conductivity. However, current processes to produce and purify Si are complex, expensive, and energy-intensive. Here, we show a nanopurification process, which involves only simple and scalable ball milling and acid etching, to increase Si purity drastically [up to 99.999% (wt %)] directly from low-grade and low-cost ferrosilicon [84% (wt %) Si; ~$1/kg]. It is found that the impurity-rich regions are mechanically weak as breaking points during ball milling and thus, exposed on the surface, and they can be conveniently and effectively removed by chemical etching. We discovered that the purity goes up with the size of Si particles going down, resulting in high purity at the sub–100-nm scale. The produced Si nanoparticles with high purity and small size exhibit high performance as Li ion battery anodes, with high reversible capacity (1,755 mAh g^{-1}) and long cycle life (73% capacity retention over 500 cycles). This nanopurification process provides a complimentary route to produce Si, with finely controlled size and purity, in a diverse set of applications.

Si | purification | nanoparticles | low grade | Li ion battery

Elemental Si has a large impact on the development of modern society, with different purities and sizes widely used for different applications (1–6). Achieving precise purity control is a crucial step in the development of semiconductor devices, because impurities alter the basic properties (mechanical, optical, electrical, and thermal) of semiconductors substantially. For example, it is well-known that silicon wafers need to be refined to a purity of 99.9999999% (wt %) (nine nines) for integrated circuits. In the case of photovoltaics, it is regarded that the purity of Si needs to be above 99.9999% (wt %) (six nines) to enable long carrier diffusion length (2, 7). Also, it has also been shown that Si nanowires and nanoparticles can provide several advantages, such as absorption enhancement, efficient carrier extraction, and reduced requirements for material quality (8–12). Si is also one of the most important materials for thermoelectrics, where both nanosize and heavy doping are necessary to effectively scatter phonons and tune the electronic properties, respectively (13–16). With rapid development in the past decade, Si has become one of the most promising candidates for lithium ion battery anode (17–26), where Si nanoparticles with purity above 99% (wt %) and sizes below 150 nm have shown very high capacity without mechanical fracture during electrochemical cycling (27–29).

Although Si, widely distributed in dusts, sands, and planets as various forms of silicates or Si dioxide, is the second most abundant element on earth, it rarely occurs as the pure free element in nature. Ferrosilicon [typically 84% (wt %) Si; ~$0.5–1.0/kg], an iron–silicon alloy primarily used by the steel industry, accounts for about 80% of the world's production of elemental Si. The production of high-purity Si that photovoltaics or electronic devices need from low-grade silicon is of high energy consumption and heavy pollution. Purification processes of Si typically involve the conversion of Si into volatile liquids (such as trichlorosilane or Si tetrachloride) or gaseous silane (30). The compounds are then separated by a distillation and transformed into high-purity Si by either a redox reaction or chemical decomposition at high temperatures. Additional steps are needed to obtain the nanostructures of Si by either top-down methods, such as lithography, or bottom-up approaches, such as chemical vapor deposition, which are all costly and complex processes. The acid etching method has been used for Si purification since as early as 1919, when metallurgical Si was crushed to expose impurity-rich regions for acid purification to make radar components during World War II. However, despite significant achievement (31–34), high purity of Si is rarely obtained, which significantly limited the applications.

Here, we start from low-cost, large-sized (~75 cm^3) ferrosilicon pieces [typically 83.95% Si, 13.09% Fe, 1.02% Al, 1.51% Ca, 0.18% Mn, and 0.06% Mg according to X-ray fluorescence (XRF); all of the contents listed are mass fraction] (Fig. 1*B*), crush them into small pieces (approximately a few $millimeters^3$), and use a scalable high-energy mechanical ball milling (HEMM) process in Ar atmosphere to mechanically break them into ferrosilicon nanoparticles (Fig. 1*C*). The sizes of these nanoparticles are controlled by the time (30–300 min) and speed (400–1,000 rpm) of ball millings. During the ball milling, we hypothesize that large ferrosilicon pieces tend to break at the impurity-rich region, which is defective and mechanically weak. This effect results in impurities being on the surface of smaller-sized Si particles (Fig. 1*A*). As the

Significance

Achieving precise purity control in semiconductors is a crucial step in the development of semiconductor devices. However, the production of high-purity semiconductors, including Si, is still of high capital cost, high energy consumption, and heavy pollution. Taking advantage of small size and large surface to volume ratio of nanomaterials, we develop a scalable and low-cost nanopurification process to produce and purify Si directly from low-grade ferrosilicon [84% (wt %) Si; ~$1/kg]. Purity as high as 99.999% (wt %) is achieved, making it one of few techniques that can achieve this high purity without any high-temperature (energy-intensive) processes. This nanopurification process opens tremendous opportunities to recover low-quality materials for commercially viable materials through an energy-efficient and inexpensive path.

Author contributions: J.Z. designed research; L.Z., B.Z., Z.L., and Y.T. performed research; Y.J., N.L., Y.H., and S.G. contributed new reagents/analytic tools; J.Z. and Y.C. analyzed data; and L.Z., J.Z., and Y.C. wrote the paper.

The authors declare no conflict of interest.

This article is a PNAS Direct Submission.

[1]To whom correspondence may be addressed. Email: jiazhu@nju.edu.cn or yicui@stanford.edu.

This article contains supporting information online at www.pnas.org/lookup/suppl/doi:10.1073/pnas.1513012112/-/DCSupplemental.

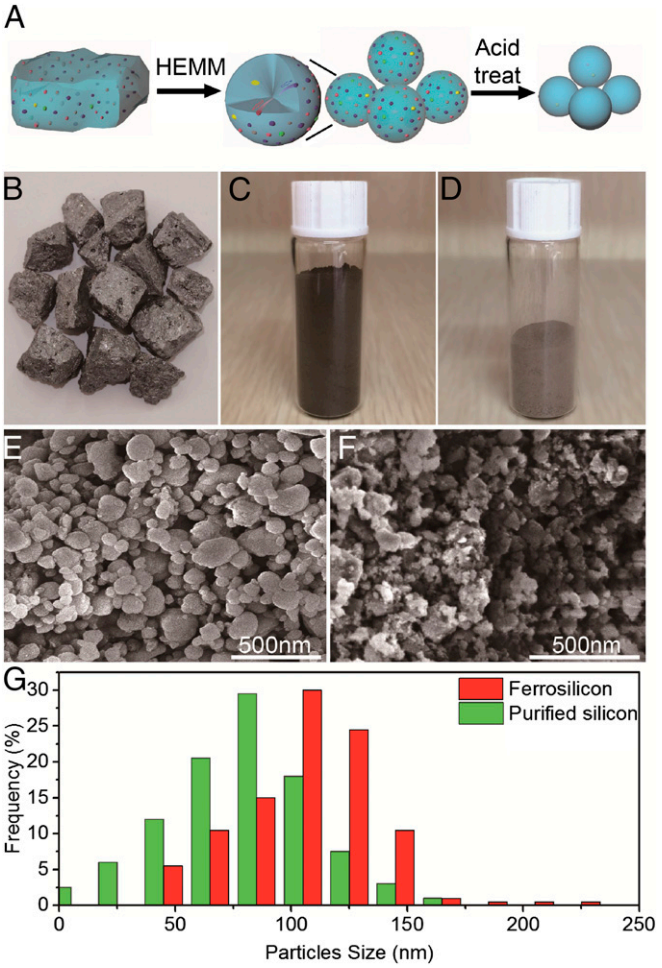

Fig. 1. The nanopurification process. (*A*) Schematic of the nanopurification process with two key steps: HEMM and acid etching. (*B–D*) Optical images of ferrosilicon bulk, ferrosilicon nanoparticles, and purified silicon nanoparticles, respectively. (*E* and *F*) SEM images of ferrosilicon nanoparticles and pure silicon nanoparticles, respectively. (*G*) Statistical analysis of the size of ferrosilicon and purified Si particles.

particle size goes down to nanoscale, the surface to volume ratio increases drastically. We expect that nearly all of the impurities would be exposed on the surface and can be effectively dissolved during acid treatment, leaving behind purified Si nanoparticles (more details are in *Methods* and Fig. 1*D*). Therefore, Si nanoparticles with different sizes and purities can be obtained without any high-temperature and energy-intensive processes. The purity as high as 99.999% (wt %) is achieved, making it one of few techniques that can achieve this high purity without any high-temperature (energy-intensive) processes.

There are two key steps to enable very high-purity Si [~99.999% (wt %)]. First, the sizes of particles need to be very small (below 100 nm) to have a large enough surface to volume ratio to efficiently expose the impurities. Second, the impurities need to be in full contact with the acid solution for enough time, so that the metal impurities can be completely removed. It is found that combinations of hydrofluoric acid (HF), nitric acid (HNO_3), and hydrochloric acid (HCl) are the best choices, because HF can remove the oxide coated on the surface of the nanoparticles, whereas HCl mixed with HNO_3 has high activity in the reaction with metal impurities (31, 35). Ultrasound is also adopted to disperse the nanoparticles in the solution and create local heating to facilitate the movement of impurities to the surface of nanoparticles (36) (more details are in *Methods*).

Fig. 1 *B–D* shows photographs of bulk ferrosilicon, ferrosilicon nanoparticles, and purified Si nanoparticles. It is noted that purified Si nanoparticles become yellowish because of the decreased size of the nanoparticles. The mass loss from bulk ferrosilicon to ferrosilicon nanoparticles during ball milling is negligible, whereas the yield from ferrosilicon nanoparticles to purified [>99.99% (wt %)] Si nanoparticles is around 60% (wt %), which is high, especially considering that ferrosilicon originally just contains about 84% (wt %) of Si. Fig. 1 *E* and *F* shows the scanning electron microscopy (SEM) images of ferrosilicon nanoparticles and purified Si nanoparticles, respectively. As indicated in Fig. 1*G*, the typical size of ferrosilicon nanoparticles is around 110 nm. After acid etching, the typical size of purified Si nanoparticles is reduced to be around 80 nm.

Fig. 2 shows transmission electron microscopy (TEM) images and electron dispersion spectroscopy mapping of ferrosilicon nanoparticles (110 nm) and purified Si nanoparticles (80 nm). As shown in Fig. 2*A*, there are significant amounts of impurities, such as Fe, Al, and Ca, in ferrosilicon nanoparticles. These impurities are effectively reduced to be below the detection limit of electron dispersion spectroscopy (<0.1%) in purified Si nanoparticles, which is shown in Fig. 2*B*. Based on the high-resolution TEM image of ferrosilicon nanoparticles, impurities, such as Fe (as a form of $FeSi_2$) and Ca (as a form of $CaSi_2$), can be easily identified, coexistent with crystalline Si (Fig. 2*C*). The crystal quality of Si nanoparticles is not compromised after acid etching, which is indicated by the high-resolution TEM in Fig. 2*D*. X-ray diffraction (XRD) patterns of the nanoparticles (*SI Appendix*, Fig. S1) also confirm the crystalline characteristics of the nanoparticles after purification processes, which is beneficial for many applications.

XRF and Inductively Coupled Plasma Mass Spectrometry (ICP-MS) are used to quantitatively investigate the level of impurities in Si at each stage and evaluate the purification effect (Fig. 3). Fig. 3*A* shows typical XRF spectra of ferrosilicon nanoparticles (~110 nm), which have clear spectra lines of the metal impurities (such as Fe, Al, Ca, Mn, and Mg). Quantitatively, the impurity levels of

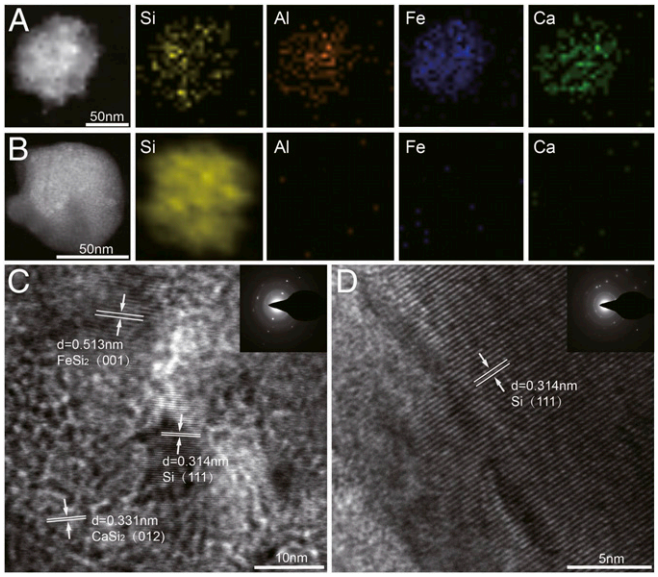

Fig. 2. TEM for elemental and structural characterizations. (*A*) TEM image and electron dispersion spectroscopy mapping of nanoparticles before the nanopurification process, (*B*) TEM image and electron dispersion spectroscopy mapping of nanoparticles after the nanopurification process. (*C*) High-resolution TEM images and diffraction pattern of nanoparticles before the nanopurification process. (*D*) High-resolution TEM images and diffraction pattern of nanoparticles after the nanopurification process.

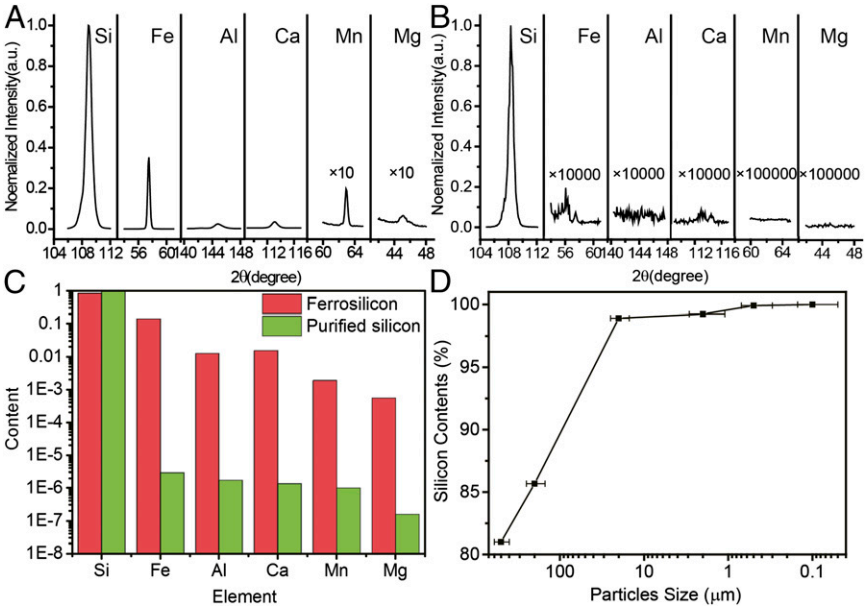

Fig. 3. Impurity analysis before and after the nanopurification process. (*A* and *B*) XRF spectra of the nanoparticles before and after nanopurification, respectively. (*C*) ICP data of the nanoparticles before and after nanopurification. Five major impurities, Fe, Al, Ca, Mn, and Mg, are listed. Other impurities are listed in *SI Appendix*, Fig. S2. (*D*) The relationship between particle size and the purity of particles.

Fe, Al, Ca, Mn, and Mg are found to be 13.09%, 1.02%, 1.51%, 0.18%, and 0.06% (wt %), respectively (Fig. 3*A*). After ball milling and acid etching, no peaks related to metal impurities can be found, even when the spectra are magnified by 10,000 times (Fig. 3*B*). Quantitatively, the impurity levels of Mn, Mg, Ti, and Cu are found to be below the detection limit of XRF (0.001%). ICP-MS results before and after acid etching further confirm the purification effect. ICP-MS results based on purified Si nanoparticles indicate that all of the metal impurities are reduced to be less than 0.001% (Fe, 0.00029%; Al, 0.00017%; Ca, 0.00014%; Mn, 0.00009%; and Mg, 0.00002%), and therefore, Si has the purity of 99.99916% (wt %) [higher than 99.999% (wt %)]. It should be emphasized that the purification effect depends strongly on the size of the particles, as shown in Fig. 3*D* (the error bar indicates the range of particles size). If the size of particles is around 500 μm, there is no obvious purification effect. Si with 99.92% (wt %) purity can be obtained when the typical size of particles is around 500 nm. This strong size-dependent purification effect can be attributed to two reasons. First, crystals tend to break at impurity-rich regions. Smaller particles have larger surface to volume ratios; therefore, there are more chances that impurities sit on the surface of particles. Second, smaller particles also provide short path lengths for impurities inside to move to the surface induced by heating during processes (more details are in *SI Appendix*). It can be expected that higher-purity Si [~99.9999% (wt %); six nines] can be obtained through this nanopurification process with smaller silicon nanoparticles or higher-purity Si sources.

X-ray photoelectron spectroscopy (XPS), which measures the kinetic energy and number of electrons that escape from the surface (~5 nm) of the materials, is used to carefully examine the distribution of impurities and confirm the purification mechanism (Table 1 and *SI Appendix*, Fig. S3). According to XPS, for bulk ferrosilicon, the contents of Fe, Al, Ca, Mn, and Mg are 9.7%, 5.4%, 3.5%, 0.2%, and 0.1% (wt %), respectively (Table 1). However, after ball milling, it is found that the contents of Fe, Al, Ca, Mn, and Mg in ferrosilicon nanoparticles increase to 12.3%, 18.2%, 6.3%, 1.3%, and 0.2% (wt %) (Table 1). Because XPS is a very surface-sensitive technique, this increase of impurities after ball milling confirms that more impurities appear on the surfaces of particles after ball milling, which is beneficial for purification processes. As indicated by XPS data of nanoparticles after acid etching, the contents of all of the metal impurities are all below the detection limit of XPS (0.1%), confirming the significant purification effect (Table 1).

This simple and scalable nanopurification process can produce Si nanoparticles with small sizes (~80 nm) and high purity [higher than 99.999% (wt %)], opening up opportunities for various applications. As an example, we showed their application as high-capacity battery anodes. We built lithium ion batteries similar to those in our previous studies (24, 27, 37) (details are in *Methods*). The results of electrochemical tests are presented in Fig. 4. On deep galvanostatic cycling between 0.01 and 1.5 V, the discharge (delithiation) capacity reached 1,755 mAh g^{-1} for the first cycle at C/20 (1 C = charge/discharge in 1 h) and remained around 1,300 mAh g^{-1} after 200 cycles at C/5 (Fig. 4*A*). All reported capacities are based on the total mass of anode (including Si, binder, and acetylene black). Because Si is about 60% of the mass of the total anode, the capacity with respect to Si is as high as 2,925 mAh g^{-1}. From the 2nd to the 200th cycle at a rate of C/5, the capacity retention was ~73%, significantly better compared with that of ferrosilicon nanoparticles. Before purification processes, the nanoparticles only contained 84% (wt %) Si, leading to a low capacity (1,396 mAh g^{-1}) at first cycle. Moreover, the presence of an impurity (mainly $FeSi_2$), which has a low conductivity (38) and a comparatively bigger size, leads to poor performance, and just 20% capacity was retained after 200 cycles. Carbon coating is used to further improve battery performance, because it can buffer the expansion of the particles during cycling and improve conductivity (37, 39). A TEM image (*SI Appendix*, Fig. S4) confirms the

Table 1. XPS characterizations of the element contents near the surface at each step of the nanopurification process

Material (wt%)	Si	Fe	Al	Ca	Mn	Mg
Bulk	81.1	9.7	5.4	3.5	0.2	0.1
After ball milling	61.7	12.3	18.2	6.3	1.3	0.2
After purification	>99.9	<0.1	<0.1	<0.1	<0.1	<0.1

CHEMISTRY

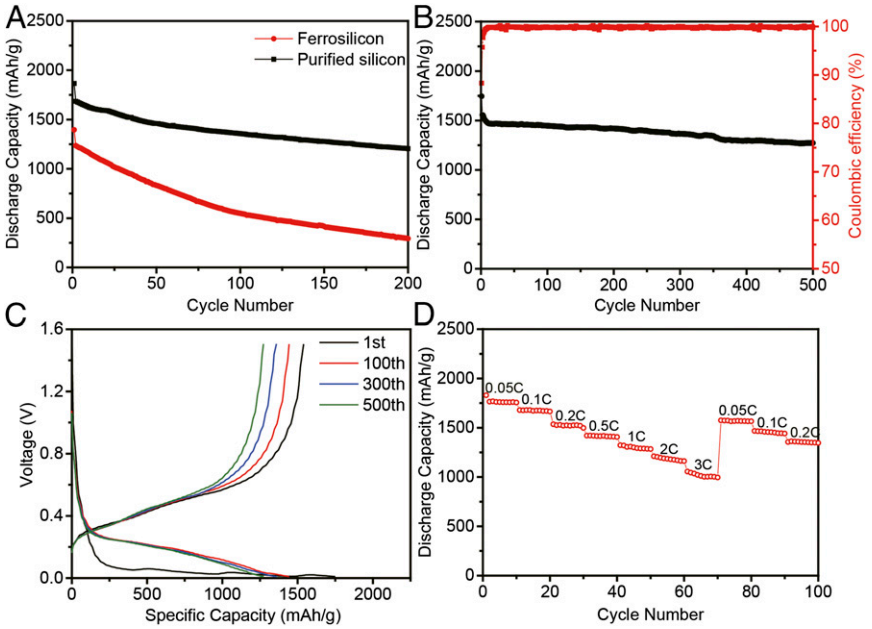

Fig. 4. Electrochemical performance. All specific capacities of silicon anodes are based on the total mass of anode. (*A*) Discharge capacity for the first 200 cycles of ferrosilicon nanoparticles and purified silicon nanoparticles. (*B*) Discharge capacity and coulombic efficiency (red) of purified silicon nanoparticles after carbon coating. (*C*) Voltage profiles for the purified silicon nanoparticles after carbon coating plotted for the 1st, 100th, 300th, and 500th cycles. (*D*) Battery performance at different rates from 0.05C to 3C.

existence of amorphous carbon coating on the surface of purified Si nanoparticles. Also, the result of thermoanalysis (*SI Appendix*, Fig. S5) indicates that the mass ratio of carbon coating is 10%. After 500 deep cycles at a rate of C/2, the capacity still remained above 1,270 mAh g^{-1}, which corresponds to a capacity decay as small as 0.05% per cycle (Fig. 4*B*). As known to all, coulombic efficiency is an important indicator of the reversibility of the electrode reaction. After carbon coating, the initial coulombic efficiency reached 88.3%, which is high for the Si anode. The coulombic efficiency increased to above 99% rapidly with subsequent few cycles, and the average coulombic efficiency from the 2nd to the 500th cycles of the carbon-coated Si nanoparticles is around 99.81% (Fig. 4*B*), indicating stable structure during cycling. The discharge–charge voltage profiles of the Si nanoparticles with carbon coating in different cycles are shown in Fig. 4*C*. The first lithiation potential shows a plateau between 0.1 and 0.01 V, consistent with the behavior of crystal Si. It is notable that, with carbon coating, the electrode showed a better rate performance. As shown in Fig. 4*D*, the capacity of Si nanoparticles varies from 1,830 to 1,000 mAh g^{-1} at a charge/discharge rate from C/20 to 3C.

In summary, we developed successfully a nanopurification process, which is composed of simple ball milling and acid etching processes, to produce Si nanoparticles with controlled size and purity up to 99.999% (wt %) directly from low-grade and low-cost ferrosilicon. We show that the small size and high purity of the obtained Si nanoparticles afford good performance as the Li ion battery anode. With additional development, we believe that it is possible to improve the purity up to six nines or higher. The nanopurification concept proposed in this study opens a previously unidentified and exciting opportunity to recover low-quality silicon for commercially viable materials and produce cost-effective energy conversion and storage devices, such as batteries, photovoltaics, and thermoelectrics.

Methods

Synthesis of High-Purity Si Nanoparticles. Ferrosilicon [84% (wt %)] was used as received to prepare high-purity Si nanoparticles by HEMM and acid treatment processes. It was first crushed into the millimeter range, and then, it was ball-milled into nanoparticles by HEMM for a few hours at a speed of 800 rpm with 3-mm grinding balls and then, 2 h at a speed of 1,000 rpm with 1-mm grinding balls. The ferrosilicon nanoparticles were then immersed in a solution of 0.5 M HF, 5 M HCl, and 5 M HNO_3 at 60 °C. An additional small amount of ethanol was added under continuous stirring to disperse the nanoparticles in the solution. After magnetic stirring, the solution was sonicated in an ultrasonic washer for 2 h. The nanoparticles were then filtered out and washed with deionized water and ethanol. For carbon coating of the purified Si nanoparticles, 1 g Si nanoparticles and 3 g citrate were dispersed in 5 mL deionized water. Next, the solution was dispersed by ultrasonic shaking and then, dried in a vacuum oven at 110 °C. Finally, the powders were carbonized under Ar atmosphere for 2 h with a rate of 5 °C min^{-1} from room temperature to 400 °C and a rate of 1 °C min^{-1} from 400 °C to 800 °C. Carbon-coated pure Si nanoparticles were immersed in 5 wt% HF aqueous solution for 30 min to remove the SiO_2 layer followed by filtration and deionized water washing three times. The final carbon-coated pure Si nanoparticles were obtained after drying in a vacuum oven.

Material Characterizations. The morphologies and structures of the as-prepared Si nanoparticles were characterized by SEM (dual-beam FIB 235; FEI Strata) and TEM (JEM-200CX). XPS spectra were obtained on THERMO FISHERSCIENTIFIC K-Alpha. X-ray diffraction spectra were obtained on a Rigaku Ultima X-Ray IV Diffractometer using a Cu K_a of 1°/min. XRF spectra were obtained on SHIMADZU XRF-1800. ICP data were obtained on SHIMADZU ICPE-9000.

Electrochemical Testing. The prepared Si nanoparticles are mixed with carbon black and carboxyl methyl cellulose (CMC) binder (3:1:1; weight ratio) to make a slurry, cast onto a thin copper foil, and dried in a vacuum oven at 90 °C overnight and 110 °C for 2 h. Coin-type cells (2032) were fabricated inside an Ar-filled glove box using Li metal foil as counter/reference electrode along with a celgard 2250 separator. The electrolyte used was 1.0 M $LiPF_6$ in 1:1 (vol/vol) ethylene carbonate:diethyl carbonate with 2% (wt %) vinylene carbonate (Guotai Huarong) added to improve the cycling stability. Galvanostatic cycling was performed using a LANHE CT2001A, and the galvanostatic voltage cutoffs were 0.01 and 1.5 V vs. Li/Li^+. The charge/discharge rate was calculated with respect to the theoretical capacity of Si (4,200 mAh/g; 1 C = 4,200 mA/g). All of the capacities reported in the manuscript were based on the whole mass of the electrode (including active materials, binder, and acetylene black). The mass loading of each electrode was ~0.2 mg/cm^2.

ACKNOWLEDGMENTS. This work is jointly supported by State Key Program for Basic Research of China Grant 2015CB659300, National Natural Science Foundation of China Grants 11321063 and 11574143, Natural Science Foundation of Jiangsu Province Grant BK20150056, the Priority Academic Program Development of Jiangsu Higher Education Institutions, and the Fundamental Research Funds for the Central Universities.

1. DMR (2006) *Thermoelectrics* Handbook Macro to Nano (CRC, Boca Raton, FL).
2. Green MA (1998) *Solar Cells: Operating Principles* (Technology and System Applications, Englewood Cliffs, NJ).
3. James D, Plummer MD (2000) *Silicon vlsi Technology* (Pearson Education, Elnet Software City, India), pp 49–91.
4. Swanson RM (2006) A vision for crystalline silicon photovoltaics. *Prog Photovolt Res Appl* 14(5):443–453.
5. Wadia C, Alivisatos AP, Kammen DM (2009) Materials availability expands the opportunity for large-scale photovoltaics deployment. *Environ Sci Technol* 43(6): 2072–2077.
6. Wang X, Song J, Liu J, Wang ZL (2007) Direct-current nanogenerator driven by ultrasonic waves. *Science* 316(5821):102–105.
7. Buonassisi T, et al. (2005) Engineering metal-impurity nanodefects for low-cost solar cells. *Nat Mater* 4(9):676–679.
8. Kayes BM, Atwater HA, Lewis NS (2005) Comparison of the device physics principles of planar and radial p-n junction nanorod solar cells. *J Appl Phys* 97(11):114302–114313.
9. Tian B, et al. (2007) Coaxial silicon nanowires as solar cells and nanoelectronic power sources. *Nature* 449(7164):885–889.
10. Garnett E, Yang P (2010) Light trapping in silicon nanowire solar cells. *Nano Lett* 10(3):1082–1087.
11. Wallentin J, et al. (2013) InP nanowire array solar cells achieving 13.8% efficiency by exceeding the ray optics limit. *Science* 339(6123):1057–1060.
12. Kelzenberg MD, et al. (2010) Enhanced absorption and carrier collection in Si wire arrays for photovoltaic applications. *Nat Mater* 9(3):239–244.
13. Hochbaum AI, et al. (2008) Enhanced thermoelectric performance of rough silicon nanowires. *Nature* 451(7175):163–167.
14. Zhu GH, et al. (2009) Increased phonon scattering by nanograins and point defects in nanostructured silicon with a low concentration of germanium. *Phys Rev Lett* 102(19): 196803.
15. Boukai AI, et al. (2008) Silicon nanowires as efficient thermoelectric materials. *Nature* 451(7175):168–171.
16. Joshi G, et al. (2008) Enhanced thermoelectric figure-of-merit in nanostructured p-type silicon germanium bulk alloys. *Nano Lett* 8(12):4670–4674.
17. Bruce PG, Scrosati B, Tarascon JM (2008) Nanomaterials for rechargeable lithium batteries. *Angew Chem Int Ed Engl* 47(16):2930–2946.
18. Su X, et al. (2014) Silicon-based nanomaterials for lithium-ion batteries: A review. *Adv Energy Mater* 4(1):1–23.
19. Goodenough JB, Kim Y (2010) Challenges for rechargeable Li batteries. *Chem Mater* 22(3):587–603.
20. Armand M, Tarascon JM (2008) Building better batteries. *Nature* 451(7179):652–657.
21. Magasinski A, et al. (2010) High-performance lithium-ion anodes using a hierarchical bottom-up approach. *Nature Materials* 9(4):353–358.
22. Jung DS, Ryou MH, Sung YJ, Park SB, Choi JW (2013) Recycling rice husks for high-capacity lithium battery anodes. *Proc Natl Acad Sci USA* 110(30):12229–12234.
23. Kasavajjula U, Wang CS, Appleby AJ (2007) Nano- and bulk-silicon-based insertion anodes for lithium-ion secondary cells. *J Power Sources* 163(2):1003–1039.
24. Chan CK, et al. (2008) High-performance lithium battery anodes using silicon nanowires. *Nat Nanotechnol* 3(1):31–35.
25. Park MH, et al. (2009) Silicon nanotube battery anodes. *Nano Lett* 9(11):3844–3847.
26. Tarascon JM, Armand M (2001) Issues and challenges facing rechargeable lithium batteries. *Nature* 414(6861):359–367.
27. McDowell MT, et al. (2012) Studying the kinetics of crystalline silicon nanoparticle lithiation with in situ transmission electron microscopy. *Adv Mater* 24(45):6034–6041.
28. Kim H, Seo M, Park MH, Cho J (2010) A critical size of silicon nano-anodes for lithium rechargeable batteries. *Angew Chem Int Ed Engl* 49(12):2146–2149.
29. Liu XH, et al. (2012) Size-dependent fracture of silicon nanoparticles during lithiation. *ACS Nano* 6(2):1522–1531.
30. Hegedus ALAS (2011) *Handbook of Photovoltaic Science and Engineering* (John Wiley & Sons, Chichester, UK), pp 169–215.
31. Yu ZL, et al. (2007) Removal of iron and aluminum impurities from metallurgical grade-silicon with hydrometallurgical route. *T Nonferr Metal Soc* 17(1B):S1030–S1033.
32. Matjie RH, Engelbrecht R (2007) Selective removal of dissolved silicon and aluminium ions from gas liquor by hydrometallurgical methods. *Hydrometallurgy* 85(2-4):172–182.
33. Lian SS, Kammel R, Kheiri MJ (1992) Preliminary study of hydrometallurgical refining of mg-silicon with attrition grinding. *Sol Energy Mater Sol Cells* 26(4):269–276.
34. Dietl J (1983) Hydrometallurgical purification of metallurgical-grade silicon. *Sol Cells* 10(2):145–154.
35. Santos IC, et al. (1990) Purification of metallurgical grade silicon by acid leaching. *Hydrometallurgy* 23(2-3):237–246.
36. Ma XD, Zhang J, Wang TM, Li TJ (2009) Hydrometallurgical purification of metallurgical grade silicon. *Rare Metals* 28(3):221–225.
37. Liu N, et al. (2014) A pomegranate-inspired nanoscale design for large-volume-change lithium battery anodes. *Nat Nanotechnol* 9(3):187–192.
38. Chen Y, Qian J, Cao Y, Yang H, Ai X (2012) Green synthesis and stable li-storage performance of FeSi(2)/Si@C nanocomposite for lithium-ion batteries. *ACS Appl Mater Interfaces* 4(7):3753–3758.
39. Cai Z, et al. (2015) Manganese oxide/carbon yolk-shell nanorod anodes for high capacity lithium batteries. *Nano Lett* 15(1):738–744.